Downloaded from specialpapers.gsapubs.org on April 9, 2015

Geological Society of America
Special Paper 407
2006

Deep seismic images of the Southern Andes

X. Yuan
G. Asch
GeoForschungsZentrum Potsdam, Telegrafenberg, 14473 Potsdam, Germany
K. Bataille
Departamento Ciencias de la Tierra, Universidad de Concepción, Concepción, Chile
G. Bock*
M. Bohm
H. Echtler
GeoForschungsZentrum Potsdam, Telegrafenberg, 14473 Potsdam, Germany
R. Kind
O. Oncken
GeoForschungsZentrum Potsdam, Telegrafenberg, 14473 Potsdam, Germany, and
Freie Universität Berlin, Malteserstraße 74-100, 12249 Berlin, Germany
I. Wölbern
GeoForschungsZentrum Potsdam, Telegrafenberg, 14473 Potsdam, Germany

ABSTRACT

Teleseismic earthquakes recorded within the ISSA (Integrated Seismological Experiment in the Southern Andes) temporary seismic experiment in the Southern Andes between 36° and 40°S latitude have been used to construct receiver function images of the crust and upper mantle. The oceanic Moho of the subducted Nazca plate is observed down to a depth of ~100 km, corresponding well with the Wadati-Benioff zone seismicity and wide-angle seismic reflections. Beneath the volcanic arc, the slab begins to be invisible with P-to-S converted waves, implying the completion of the gabbro-eclogite transformation in the oceanic crust at that depth. The continental Moho has been imaged at depth of ~40 km beneath the main cordillera and shallows toward the eastern end of the profile beneath the Neuquén Basin to ~35 km depth. Beneath the Loncopué graben, the Moho is locally uplifted to 30 km depth, possibly resulting from the backarc spreading beginning in the Pliocene-Pleistocene. An anomalously high Poisson's ratio beneath the volcanic arc may indicate partial melting in the upper-plate crust.

Keywords: Southern Andes, subduction zone, P-to-S conversion, receiver function, Moho, slab.

*Deceased (6 November 2002).

Yuan, X., Asch, G., Bataille, K., Bock, G., Bohm, M., Echtler, H., Kind, R., Oncken, O., and Wölbern, I., 2006, Deep seismic images of the Southern Andes, *in* Kay, S.M., and Ramos, V.A., eds., Evolution of an Andean margin: A tectonic and magmatic view from the Andes to the Neuquén Basin (35°–39°S lat): Geological Society of America Special Paper 407, p. 61–72, doi: 10.1130/2006.2407(03). For permission to copy, contact editing@geosociety.org. ©2006 Geological Society of America. All rights reserved.

Downloaded from specialpapers.gsapubs.org on April 9, 2015

INTRODUCTION

The Andean orogenic belt, stretching for more than 7000 km along the western margin of South America, was formed during the Cenozoic from convergence of the oceanic Nazca plate and the South American plate. It displays distinct along-strike variations in subduction geometry, arc volcanism, and orogenic shortening (Cahill and Isacks, 1992; Ramos, 1999). Defined by the Wadati-Benioff zone, the dip of the subducted Nazca plate changes several times between normal subduction with angles of 20°–30° and segments of flat subduction with angles of ~10°. The variation of the subduction geometry from north to south is directly related to four active volcanic zones: the Northern (5°N–2°S), Central (16°S–26°S), Southern (34°S–46°S), and Austral (south of 47°S) volcanic zones. All these volcanic zones are located in the normal subduction zones, separated by flat subduction zones without volcanic activity. The Andean orogenic belt varies both in width and elevation among different volcanic zones. In the Central Andean volcanic zone, the orogenic belt is the broadest, with a width of >800 km. Subduction and continental deformation has created two significant plateaus, the Altiplano and Puna at 3.8 and 4.5 km elevation, respectively. The maximum elevation is more than 6000 m. The Wadati-Benioff zone reaches a depth of more than 650 km (Cahill and Isacks, 1992). In the Southern volcanic zone, the mountain belt is much narrower and lower. The mean elevation is <1500 m. The subduction zone seismicity here is much less, and the Wadati-Benioff zone only reaches 200 km depth.

These major differences of the surface expression between the Central and the Southern Andean mountain belt point to different architectures of the system and different processes at depth. While the Central Andes have been extensively studied with diverse seismic experiments (e.g., Beck et al., 1996; Yuan et al., 2000; ANCORP Working Group, 2003), little is known about the deep seismic structure of the Southern Andes. Several short industry reflection lines have been imaged mainly the upper crust in the study area (Jordan et al., 2001). Within the collaborative Research Project SFB (Sonderforschungsbereich) 267 "Deformation Processes in the Andes," an array of broadband seismographs and a network of short-period seismic stations have been deployed in the Southern Andes (Fig. 1). The 450-km-long east-west array roughly along 39°S latitude from the Pacific coast into the Neuquén Basin, consisting of 13 broadband seismic stations equipped with Guralp 3ESP's and SAM data loggers, was deployed from April 1999 to November 2001. The broadband array was planned for a teleseismic receiver function study. The additional short-period network consisted of 62 seismic stations, equipped with 1 Hz Mark or 5 s MarsLite seismometers and PDAS, MarsLite, and Orion data loggers. It was in operation for ~100 d between January and April 2000, covered an area of 400 × 550 km, and was designed to improve the images of local seismicity and seismic tomography using local earthquakes (Bohm et al., 2002). In addition to the passive-source seismic experiments, a seismic refraction profile with four shots was executed along the broadband array (Bohm et al., 2002; Lüth et al., 2003).

The onshore morphotectonic segmentation of the Southern Andes comprises a forearc, integrating the Coastal Cordillera and the Central Valley, and the Main Cordillera and Neuquén Basin (Fig. 1). The longitudinal depression of the Central Valley contains up to several kilometers of sediments and has been an active extensional depocenter since the late Oligocene (Muñoz et al., 2000; Jordan et al., 2001). The Main Cordillera, with mean altitudes steadily decreasing from ~2700 m at 36°S to <~1000 m at 41°S, is the main morphologic component of the Andean orogen. It includes the southern active volcanic arc (Hildreth and Moorbath, 1988), which is characterized by long-lived, stationary (relative to the trench) magmatic activity that has persisted since the Jurassic. The backarc area to the east is dominated by the Neuquén Basin, which formed in a continental embayment as an active depocenter during the Late Triassic to Late Cretaceous (Franzese et al., 2003; Ramos et al., 2004; Ramos and Folguera, 2005;). The basin was inverted during the Late Cretaceous and late Miocene into a fold-and-thrust belt with only moderate shortening compared with the sub-Andean system of the Central Andes (Ramos, 1978). Between the Neuquén Basin and the Main Cordillera, the Loncopué graben formed during the Pliocene to the Quaternary as a result of backarc extension.

In this paper, we use the receiver function method to study the shear velocity structure, especially discontinuities, in the crust and upper mantle beneath the seismic stations down to the depth of the mantle transition zone. The broadband station array had a longer operation period and therefore contributed most of the data set. Besides the local earthquakes recorded at the short-term network stations, a number of teleseismic earthquakes were also recorded within the operation period. The data quality was, however, not sufficient to study the along-strike structural variations. The data processing and interpretation were mainly focused on the broadband array along 39°S latitude.

DATA AND METHODS

Receiver function analysis has become a routine method for studying crust and upper-mantle discontinuities (Langston, 1977; Vinnik, 1977). It can detect discontinuities beneath seismic stations by identifying P-to-S converted waves at these discontinuities. The converted S waves travel slower to the stations than the direct P wave does, and therefore, will be recorded after the direct P wave in the P wave coda. With the receiver function technique, we can identify these mode conversions and measure the differential time between the converted S and the direct P waves. The weak conversion energy (only a few percent of the P wave energy) can be isolated from the P wave with receiver function analysis, which includes coordinate rotation and deconvolution. Except for the primary conversions (Ps), multiple phases like PpPs and PpSs, which reverberate between the discontinuity and Earth's surface, can frequently be observed

Downloaded from specialpapers.gsapubs.org on April 9, 2015

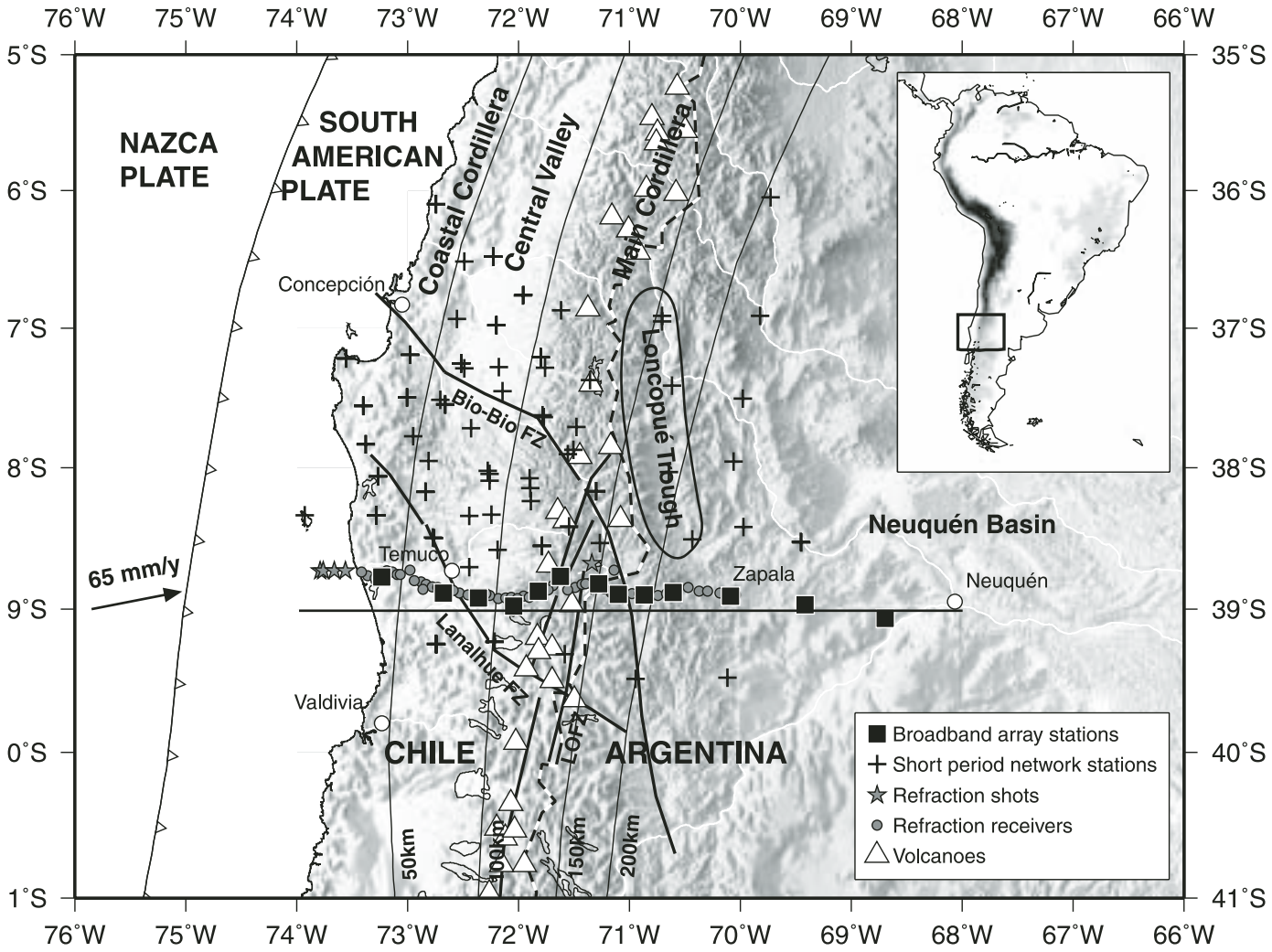

Figure 1. Map of stations in the Southern Andes between 36° and 40°S latitude. The recent convergence rate between the Nazca plate and South American plate is 65 mm/yr (Angermann et al., 1999). Slab contours (Gudmundsson and Sambridge, 1998) mark the subducted oceanic lithosphere. Major active faults and structures are included (LOFZ—Liquiñe Ofquí fault zone [FZ]). Young volcanoes are marked by white triangles. The E-W line at latitude 39°S shows the position of the receiver function cross section.

(Fig. 2). The multiples are weaker than the Ps wave because of scattering on their longer ray paths, and so they are sometimes difficult to identify. The multiples have a different distance dependence (moveout) and thus can be distinguished from the Ps phase. Recognition of the crustal multiples helps to accurately estimate crustal thickness and the average crustal Vp/Vs ratio (Zandt et al., 1995; Zhu and Kanamori, 2000; Kind et al., 2002).

To calculate receiver functions, teleseismic waveform data of P and PP phases with high signal/noise ratios have been selected. We used P waveforms of earthquakes with epicenter distances ranging from 30° to 95° and magnitudes (mb) larger than 5.5. The PP waveforms have been selected for epicenter distances between 70° and 180° and magnitudes larger than 6.0. Figure 3 shows the location of the 67 earthquakes used in this study. Most of the earthquakes were located in the Central

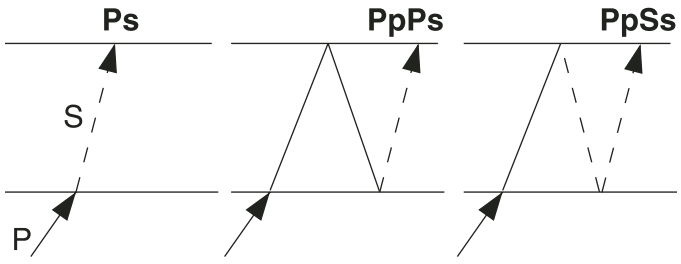

Figure 2. Ray paths of the directly converted Ps wave (transmission) and the multiple reverberations (reflection) of PpPs and PpSs waves.

Downloaded from specialpapers.gsapubs.org on April 9, 2015

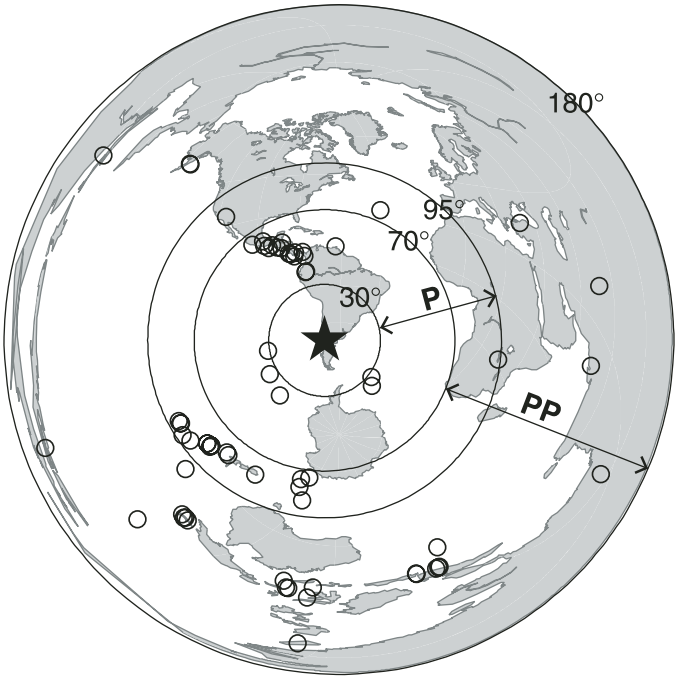

Figure 3. Locations of teleseismic earthquakes used in this study. Earthquakes with epicenter distances between 30° and 95° have been selected for P wave analysis. Earthquakes with larger distances (70° to 180°) were used for PP waves.

America and Fiji-Tonga subduction zones, with back azimuths of northwest and southwest, respectively.

Receiver functions for each earthquake-station pair were calculated using the method described by Yuan et al. (1997). Three-component seismograms were rotated into an LQT ray-oriented coordinate system, in which the L component is in the direction of the incident P wave; the Q component is perpendicular to the L component and is positive away from the source (in SV direction); and the T component is the third component of the LQT right-hand system (in SH direction). The L component is dominated by the P wave, while the Q and T components contain mainly the converted S wave energy. For horizontally layered homogeneous media, the converted S wave energy is exclusively contained in the Q component. The presence of significant energy on the T component indicates laterally varying and/or anisotropic structures. The rotation angles (back azimuth and incidence angle) were determined by the eigenvalues of the covariance matrix over a time window spanning the first few seconds following the P wave arrival. Receiver functions were computed by deconvolving the P waveforms on the L component from the corresponding Q components. A time domain deconvolution procedure was used. First, an inverse filter in the time domain was generated by minimizing the least-square difference between the observed L component and the desired delta-like spike function of normalized amplitude. Then, the inverse filter was convolved with the rotated three-component seismograms. After deconvolution, all components were normalized to the maximum amplitude of the spike on the L component to preserve the absolute amplitude of conversion ratios. A total of 340 receiver functions were obtained with the broadband array, and a similar amount of receiver functions with the short-period network stations.

OBSERVATIONS

The Upper-Mantle Discontinuities

The receiver functions have been migrated in an east-west section roughly along the plate motion direction of the subducted Nazca plate (Fig. 4). The amplitudes of receiver functions have been back-projected within one Fresnel zone along the ray path of the incident P wave. The IASP91 model (Kennett and Engdahl, 1991) was used to calculate the time-to-depth transformation. A spatial smoothing window of 20 km was applied over the section to enhance the phase correlation of the upper-mantle discontinuities. Positive amplitudes in Figure 4 (red) mark shear velocity contrast with increasing velocity downward, whereas negative amplitudes (blue) indicate layers with reduced shear wave velocity. Figure 4 shows an overall view of the major features beneath the study area, and the significant events are marked. The continental Moho can be observed by the primary conversions at a depth of ~40 km with lateral topography. A band of energy of multiple reflections within the continental crust can be seen between apparent depths of 120 and 200 km. The subducted oceanic slab, linked with the Wadati-Benioff zone seismicity, can be observed down to a depth of ~100 km. The 660 km upper-mantle discontinuity (the "660") can be clearly seen at depth of ~650 km. The 410 km discontinuity (the "410") is weakly visible in the summation trace at a depth of ~400 km. The stability of the observations of the "410" and the "660" is presented in Figure 5, where receiver functions have been stacked in order to compare effects of varied parameters. The signal from 660 km depth can be detected in nearly all of the summation traces. In the majority of cases, converted phases from 410 and 520 km depth can also be seen, but are less pronounced in general. The results indicate that not only are the "410" and "660" stable observations, but the "520" (Shearer, 1990; Helffrich, 2000) is also observed.

The 410 and the 660km discontinuities, marking the top and bottom of the mantle transition zone, are generally accepted to be phase changes in mantle mineralogy due to pressure and temperature variations in the mantle. The "410" marks the transformation from olivine to alpha-spinel, and the "660," the transformation from beta-spinel to perovskite + magnesiowustite (see Helffrich, 2000, for review). Both reactions are sensitive to temperature variation and have Clapeyron slopes of opposite signs. Variations in the discontinuity depths will, therefore, reflect mantle temperature variations; a thicker transition zone is indicative of an anomalously lower temperature, while a thin transition zone would indicate high temperatures. Our data sample the mantle transition zone west of the downgoing slab.

Downloaded from specialpapers.gsapubs.org on April 9, 2015

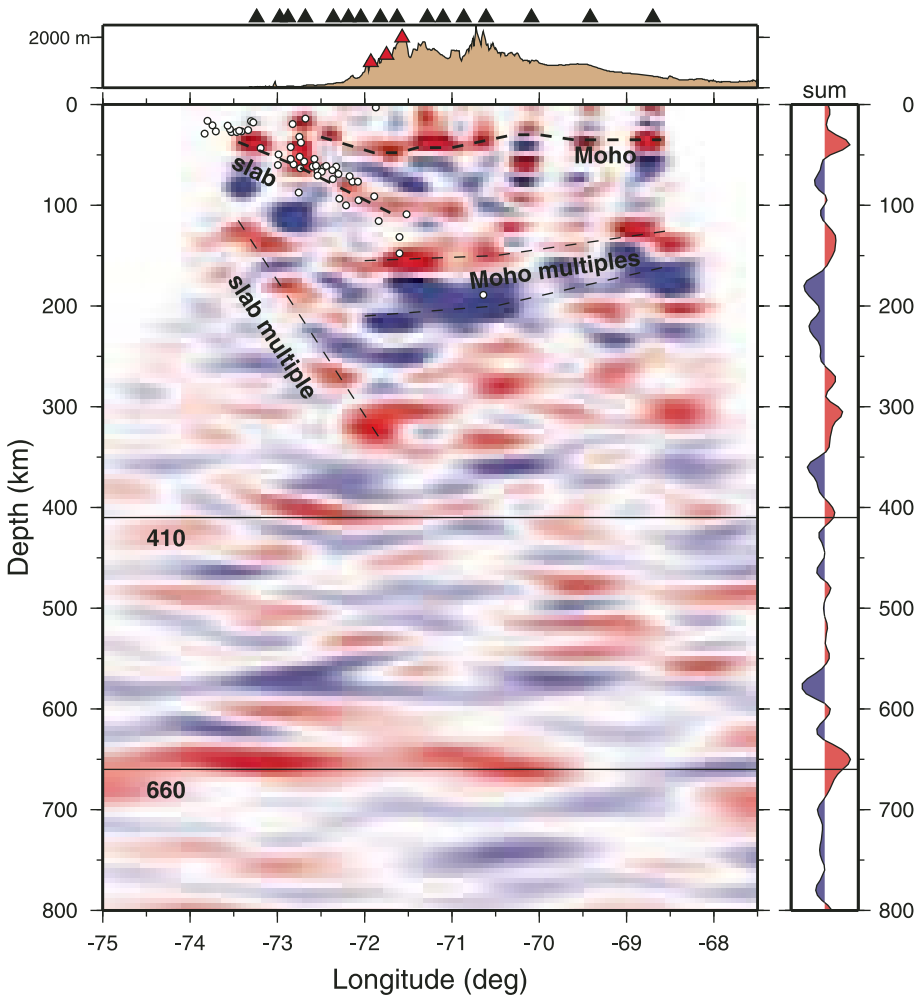

Figure 4. East-west section of receiver function image across the Southern Andes down to a depth of 800 km. Red color denotes the positive amplitudes (positive velocity jump downward) and blue denotes the negative amplitude (negative velocity jump). The main features have been marked with lines and labels. Solid lines at 410 and 660 km depth mark the global average depths of the 410 and 660 km discontinuities. Circles denote the seismicity between 38° and 40°S latitude. These earthquakes were recorded and located with the short-period mobile network (Bohm et al., 2002). The surface topography along 39°S latitude is plotted at the top. Black triangles mark the broadband stations; red triangles denote the volcanic arc. On the right is shown the summation of the receiver function image, which emphasizes horizontal structures over the entire region.

Because there are no deep earthquakes in this region, teleseismic tomography might help us to define the slab geometry in the deeper part. Although the resolution of the global teleseismic tomography in this region is relatively poor, it is still possible to see that the high-velocity oceanic lithosphere is subducted east of our sampling region at depths of the mantle transition zone (Spakman, 2004, personal commun.). In Figures 4 and 5, both the "410" and the "660" appear to be uplifted by ~10 km (or ~1 s), while the thickness of the mantle transition zone is consistent with the IASP91 model. The apparent discontinuity depth changes should be related to the velocity variations in the upper mantle above the discontinuities. The cold subducted oceanic lithosphere of higher seismic velocity increases the average upper-mantle velocities, causing the earlier arrivals of the P-to-S conversions of the discontinuities by ~1 s. The thickness of the mantle transition zone is not influenced by velocity heterogeneity in the upper mantle. The normal transition zone thickness indicates that there is no temperature anomaly in the mantle transition zone beneath our array.

The Oceanic and the Continental Moho

More details can be seen in close-up sections down to a depth of 150 km (Fig. 6). In Figure 4, we observe not only primary converted waves for both the slab and the continental Moho, but also the multiple reflection conversions, as explained

Downloaded from specialpapers.gsapubs.org on April 9, 2015

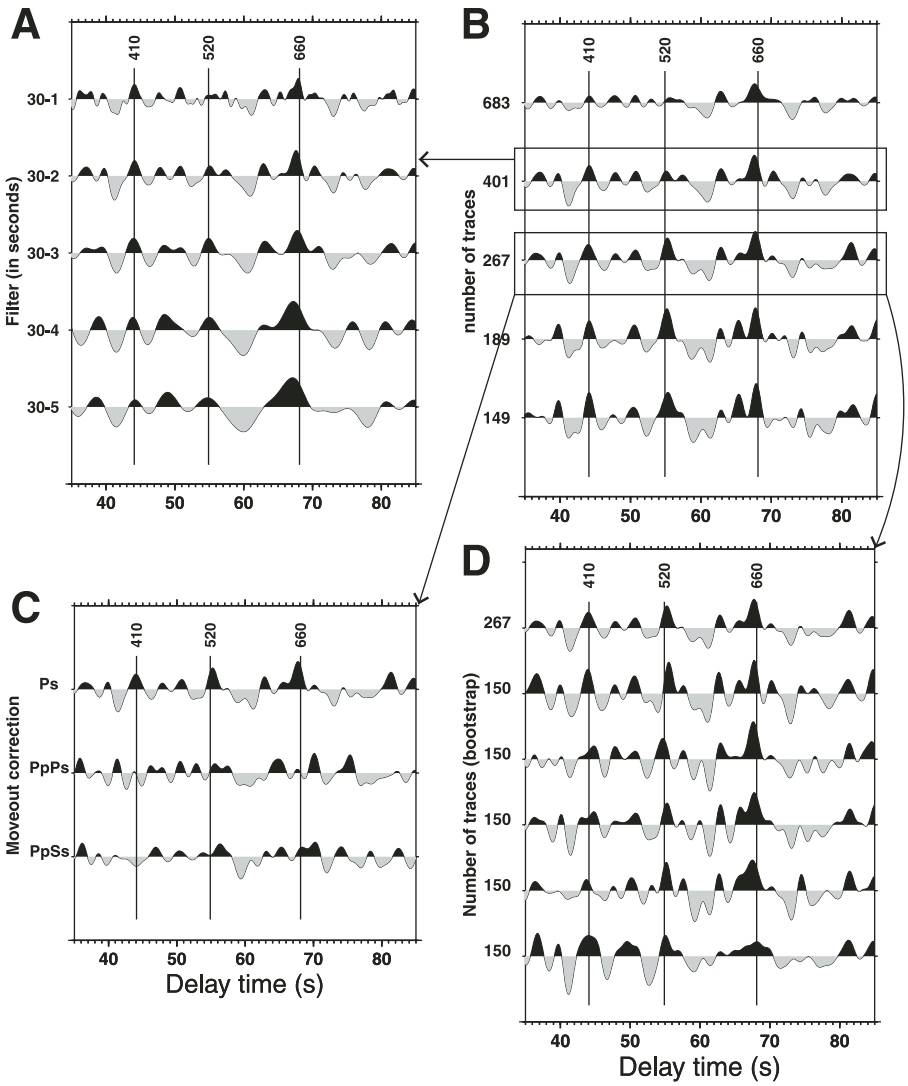

Figure 5. Summation traces showing converted phases from the mantle transition zone. Theoretical arrival times (in reference to the IASP91 model) of Ps conversions at 410, 520, and 660 km depth are marked by thin lines. (A) Varying frequency filters (bandpass is given on the left in s) have been applied. While the 660 discontinuity broadens, the 410 discontinuity disappears using more long-period filters. (B) Data set has been reduced by increasing signal-to-noise ratio. A 2–30 s bandpass filter has been applied before stacking. By removing lower-quality data, converted phases become more distinct, in particular the 410 and the 520 discontinuities, which are invisible in the complete data set. (C) Data have been corrected for moveout of the direct converted (Ps) and two multiple (PpPs, PpSs) phases prior to stacking. The upper-mantle discontinuities can be identified in the Ps-corrected summation trace. (D) Randomly selected subsets of 267 single traces have been stacked to check the stability of observations (bootstrap method).

in Figure 2. The presence of crustal multiples provides a mean for determining average crustal Vp/Vs along the profiles (Zandt et al., 1995; Zhu and Kanamori, 2000; Kind et al., 2002), further constraining the accuracy of the Moho depth estimate. Similar to Kind et al. (2002), we constructed images using the primary conversions and the multiples. Figure 6A–C shows images of the slab and the continental Moho in which the data has been back-projected assuming all the energy originated from the indicated phase (Fig. 6A—Ps, Fig. 6B—PpPs, Fig. 6C—PpSs). In each panel, only energy from the indicated phase has been migrated correctly to the approximate places, whereas all other energy would not be correctly migrated. It is clear that both the slab and the continental Moho have been reconstructed by all three kinds of phases (Ps, PpPs, and PpSs), although there are differences in depth among these events. The depth differences among different phases can be attributed to the variations

Downloaded from specialpapers.gsapubs.org on April 9, 2015

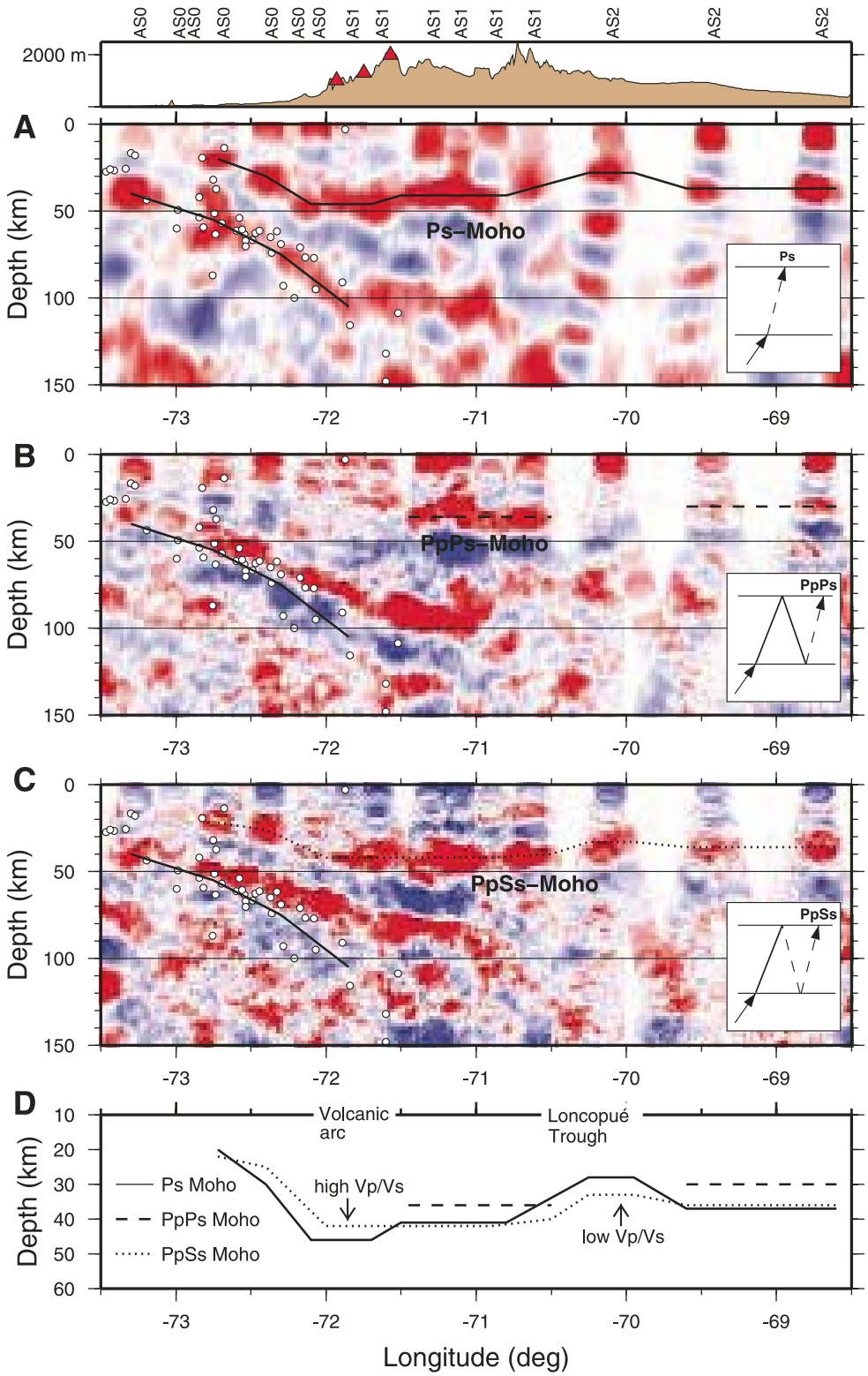

Figure 6. East-west section of the crust and the uppermost mantle down to a depth of 150 km migrated by directly converted phases (Ps) (A) and two multiples (PpPs and PpSs) (B and C). Average crustal Vp of 6.0 km/s and Vp/Vs of 1.73 were used. The continental Moho imaged with each wave type is marked in the corresponding panel with different line styles. The solid line on the slab event in each panel marks the direct Ps conversion. In each panel, the energy from the indicated phase should, in principle, have migrated correctly, whereas all other energy should be mispositioned. The observations of the continental Moho from A, B, and C are plotted in D for comparison. If there are no lateral variations in crustal Vp/Vs, the Moho images generated by each phase should mimic each other. A deeper Ps-Moho indicates a higher crustal Vp/Vs ratio, and vice versa.

Downloaded from specialpapers.gsapubs.org on April 9, 2015

in Vp/Vs ratio along the section and the dip of the structures. The back-projection can be biased when dipping interfaces exist. The ray-path deviation for reflected waves caused by dipping interfaces is roughly twice as much as that for transmitted waves; therefore, comparable to the reflection seismics, primary converted waves are less biased by dipping interfaces, whereas errors of migrated multiples at dipping interfaces might be relatively large. This is the reason for the different location of the slab in Figures 6B and 6C. Since the Moho is relatively flat, the difference between main phase and multiples can be interpreted with variations in the Vp/Vs ratio.

The subducted Nazca plate can be followed with primary P-to-S converted waves to a depth of 100 km. This phase correlates well with the Wadati-Benioff zone seismicity recorded by the short-period seismic network (Bohm et al., 2002). Coherent slab energy disappears deeper than 100 km, which is also in accordance with the pattern of the earthquake foci, which shows the termination of the intermediate-depth seismicity at the same depth. Similar observations were obtained in the Central Andes (Yuan et al., 2000). We interpret this phase as the oceanic Moho of the downgoing Nazca plate.

We picked the times of the continental Moho at the maximum of their conversion signals in Figure 6A–C, and all these "raw" depths are plotted in Figure 6D. The Moho has been continuously imaged by the Ps and PpSs phases, while the PpPs-Moho only shows two patches with relatively large depth differences compared to the other two phases. In two areas, there are large differences between the Ps- and the PpSs-Moho, where the crustal Vp/Vs ratio is apparently significantly different from the value of 1.73 used in the migrations. Beneath the arc, the Ps-Moho is deeper than the PpSs Moho, while beneath station AS20, located in the Loncopué graben, the Ps-Moho is shallower than the PpSs-Moho. We used a grid-search algorithm introduced by Zhu and Kanamori (2000) to search for crustal thickness and the average Vp/Vs ratio at some sample places. Figure 7 shows results for four subregions: the arc, backarc, the Loncopué graben, and Neuquén Basin. Except beneath the Loncopué graben, where the crustal Vp/Vs ratio is normal to low (1.68), all the other subregions show relatively high Vp/Vs ratios (>1.77). Beneath the arc, the Vp/Vs ratio is extremely high (1.89).

The estimated crustal Vp/Vs ratios were used to correct the migrated Moho image (Fig. 8). The results show that the thickness of the Andean crust is ~40 km under the arc cordillera and thins both to the west and to the east. The crust in the Neuquén Basin is approximately 34 km thick. At ~70°W, beneath the Loncopué graben, the crust is thinned by 3–4 km. To the west, the Moho can be traced to ~72.5°W to a depth of 35 km and may be followed to a depth of ~25 km beneath station AS05, where the Lanalhue fault zone is located.

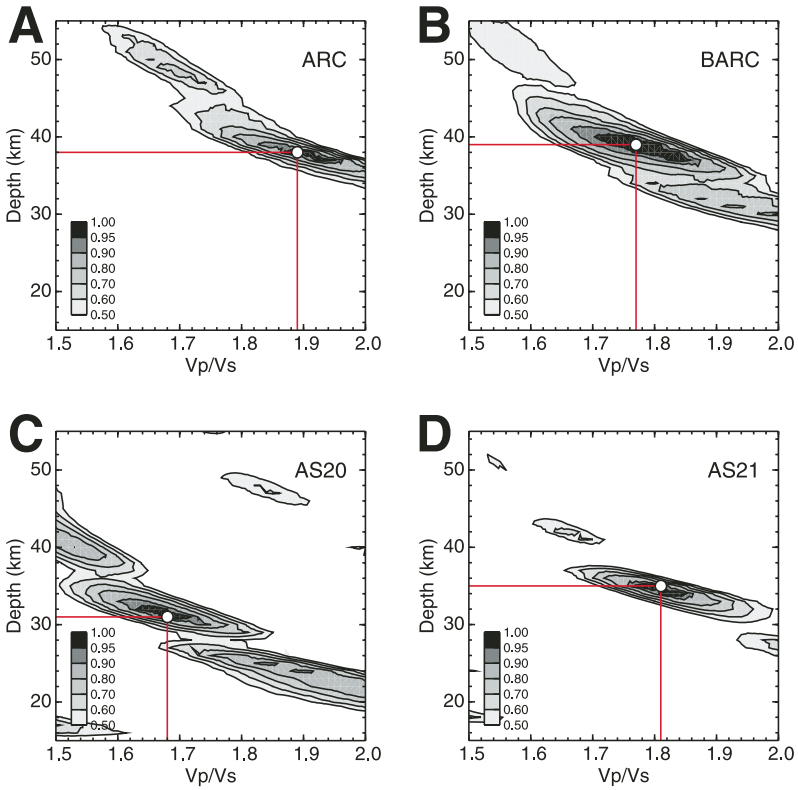

Figure 7. Grid-search for crustal thickness and Vp/Vs ratio by optimally stacking receiver functions in regions of the volcanic arc (A), backarc (B), Loncopué graben (C), and Neuquén Basin (D).

Downloaded from specialpapers.gsapubs.org on April 9, 2015

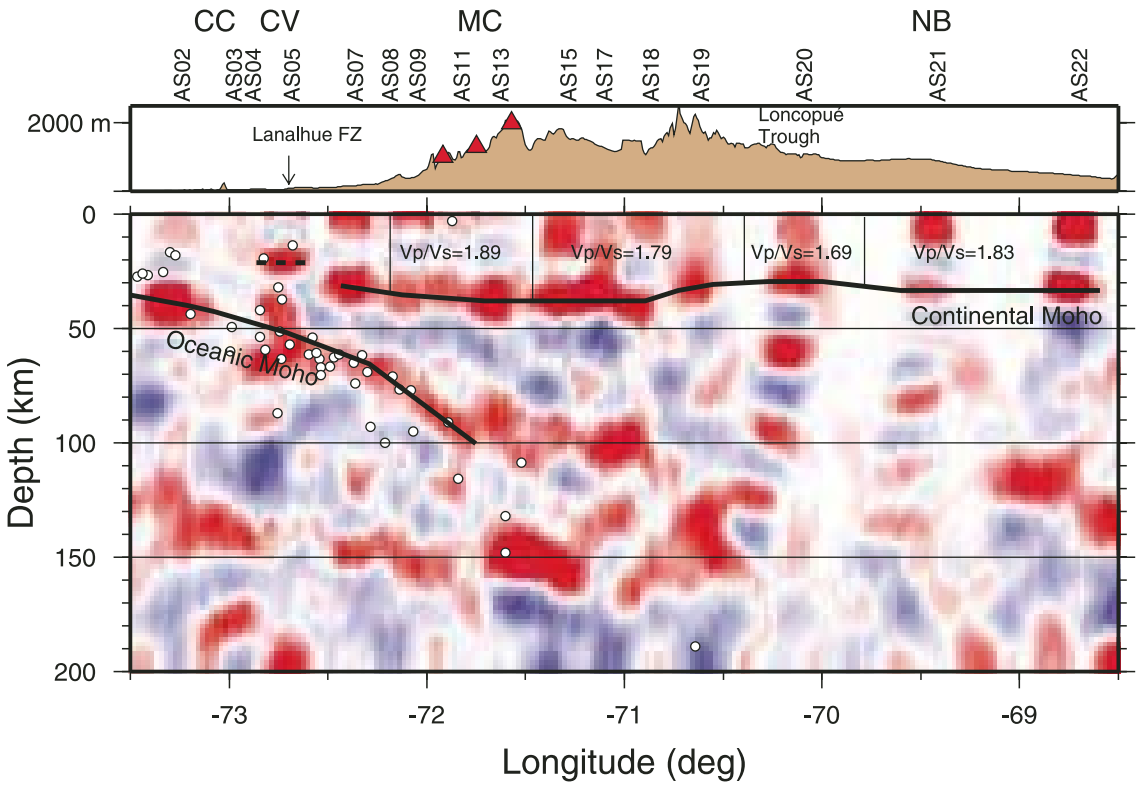

Figure 8. East-west section of the crust and the uppermost mantle with corrected Vp/Vs ratios along the section shown in the figure. Thick solid lines draw through the maximum amplitudes of the Moho and the slab conversions. The labels on the top mark the tectonic units: CC—Coastal Cordillera, CV—Central Valley, MC—Main Cordillera, and NB—Neuquén Basin. FZ—fault zone.

Crustal Thinning in the Loncopué Trough

Beneath station AS20, between 71° and 70°W longitude, the Moho shallows to a depth of ~30 km. The Moho uplift also appears to be visible at station AS19, ~50 km to the west. Grid search analysis of station AS20 shows that the crust is 31 km thick with an average Vp/Vs ratio of 1.68 (corresponding to a Poisson's ratio of 0.226) (Fig. 7C). In Figure 9A, we show the individual receiver functions of station AS20. The amplitudes at ~2 s (labeled S) relate to a near-surface low-velocity layer (sediments). The converted energy of the Moho is at 3–4 s (M). The PpPs multiple (MM) can be partly seen at a time of 13 s. The energy at 7 s (X) following the Moho conversion may have been caused by intracrustal multiples or an original conversion in the uppermost mantle at 60–70 km depth (an interpretation of similar waveforms was discussed by Mohsen et al., 2004). However, a confident interpretation with the few data presented here cannot be achieved. Figures 9B and 9C show an attempt to model the receiver functions with a simple velocity structure. The model consists of a 31-km-thick crust with a 1.5-km-thick sediment layer. A crustal Vp/Vs ratio of 1.68 was taken from the grid-search algorithm (Fig. 7C). Figure 9C shows a good match between the data (solid line) and the synthetic receiver function (dotted line). The amplitudes at 7 s (X) could be modeled better when we introduced an additional interface in the crust or the uppermost mantle. However, since we had only one station in the Loncopué graben, this could not be done very reliably.

DISCUSSION AND CONCLUSION

In Figure 10, we compare the receiver function data with seismic tomography using local earthquakes (Bohm, 2004) and wide-angle reflections (Bohm et al., 2002; Lüth et al., 2003). Receiver functions are normally used to detect interfaces with relatively sharp shear velocity contrast. The mantle lithosphere itself, seen by the low-resolution seismic tomography or surface wave dispersion analysis, is hard to see in receiver functions. When low-seismic-velocity oceanic crust exists on the top of the downgoing lithosphere, the contrast between different materials is increased and thus becomes clearly visible by receiver functions. We observed the oceanic crust to a depth of 100 km. This easterly dipping event correlates well with the wide-angle reflection (Bohm et al., 2002; Lüth et al., 2003), with the Wadati-Benioff zone seismicity (Bohm et al., 2002), and with the high-velocity zone in the seismic tomography (Bohm, 2004). Coherent slab energy begins to disappear at a depth of 100 km, as does the intermediate-depth seismicity. At the surface, this location is traced by the active volcanic arc. All this evidence

Downloaded from specialpapers.gsapubs.org on April 9, 2015

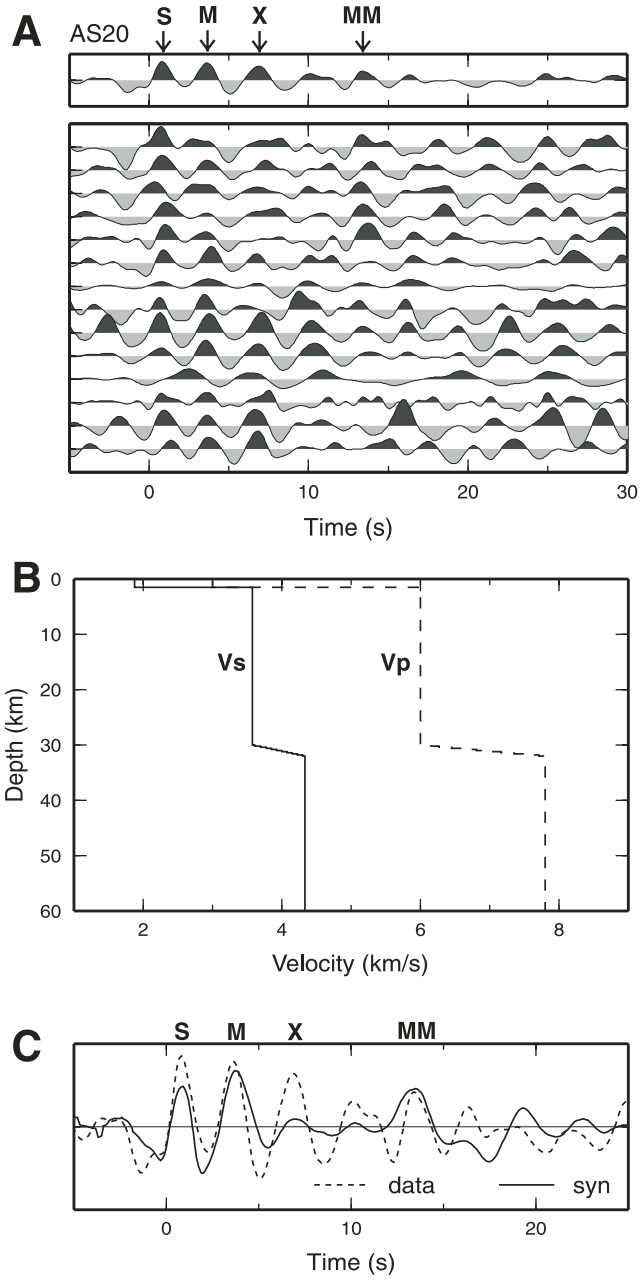

Figure 9. Individual receiver functions at station AS20 (A) and a suggested simple model (B) that matches the data well (C). S—Sediment, M—Moho, X—unknown, MM—Moho multiple.

suggests that the dipping structure represents the oceanic Moho of the downgoing Nazca plate. When it is subducted, the oceanic crust is subject to metamorphism and dehydration, which causes earthquakes (Kirby et al., 1996). With increasing pressure, basalt/gabbro in the subducted crust transforms to eclogite. At ~100 km depth, this process is probably completed. Beyond the stability limit of key hydrous phases in the basaltic and gabbroic layers (i.e., amphibole to eclogite transformation), the eclogitization will lead to a comparable seismic velocity as the surrounding mantle. This causes the oceanic crust to be seismically indistinguishable from the peridotitic mantle. In our data, this transformation appears to be completed at a depth of 100 km, beneath the volcanic arc, which is equivalent to observations in the Central Andes (Yuan et al., 2000). The metamorphism is accomplished by dehydration and fault activation in the oceanic crust, triggering the intermediate-depth earthquakes. Water released from the slab causes partial melting in the overlying mantle and forms the volcanic arc. The extremely high Poisson's ratio in the crust is consistent with large amounts of fluid and magma accumulation in the crust beneath the volcanoes (ANCORP Working Group, 2003).

It is worth noting that a subhorizontal phase with positive polarity (high velocity) at a depth of ~100 km can be clearly seen east of the subducted slab (Fig. 10, red dashed line). The phase can be traced for ~100 km to the east from the place where the slab conversions begin to disappear and the Wadati-Benioff seismicity shuts off. Looking at the slab imaged by the multiple reflections in Figures 6B and 6C, a bending of the slab converter at the tip of the slab is remarkable, suggesting that this subhorizontal phase at the end of the slab converter could be a real feature. This interface, however, cannot be the continuation of the slab that bends subhorizontally, because the intermediate-depth seismicity does not match. We speculate that the subhorizontal interface might be a remnant of the old flat slab. From the Late Cretaceous until present, the Nazca plate has changed its subduction angle several times (Ramos and Folguera, 2005; Ramos and Kay, this volume, chapter 1). The last flat subduction history was in the late Miocene (Kay et al., this volume, chapter 2). While the slab was steepening afterward in the Pliocene, a piece of subducted flat slab may have remained within the lithosphere. Alternatively, the interface might represent a hydration front in the mantle wedge, or it may be caused by some hydrous minerals floating away from the slab.

The upper-plate continental Moho is easily observed at a depth ranging between 30 and 40 km across much of the section. Compared with the moderate crustal thickness of the Central Andes, the section shows a remarkable Moho topography that can be correlated with the major morphotectonic features at the surface. The crust is ~40-km-thick beneath the arc and the transition to the backarc, and thins to the east in the Neuquén Basin (~35 km), as well as to the west in the transition to the forearc (~35 km). The relative crustal thickening of the Main Cordillera segment (40 km) in relation with the eastern hinterland (34–35 km) fits well with the mean topographic elevation of ~1400 m. Though the Moho farther west is not resolved, crustal thickness values may be as small as 25 km below the Central Valley. However, this transition to the active forearc wedge also coincides with the prominent Lanalhue fault zone (Fig. 1). This inherited pre-Andean and repeatedly reactivated discontinuity correlates with clusters of earthquakes that connect to the slab seismicity (Fig. 6). A series of scattered arrivals can be seen at depths of 25 km, 45 km, and 65 km (Fig. 10), interfering with the slab conversion event. This may indicate

Downloaded from specialpapers.gsapubs.org on April 9, 2015

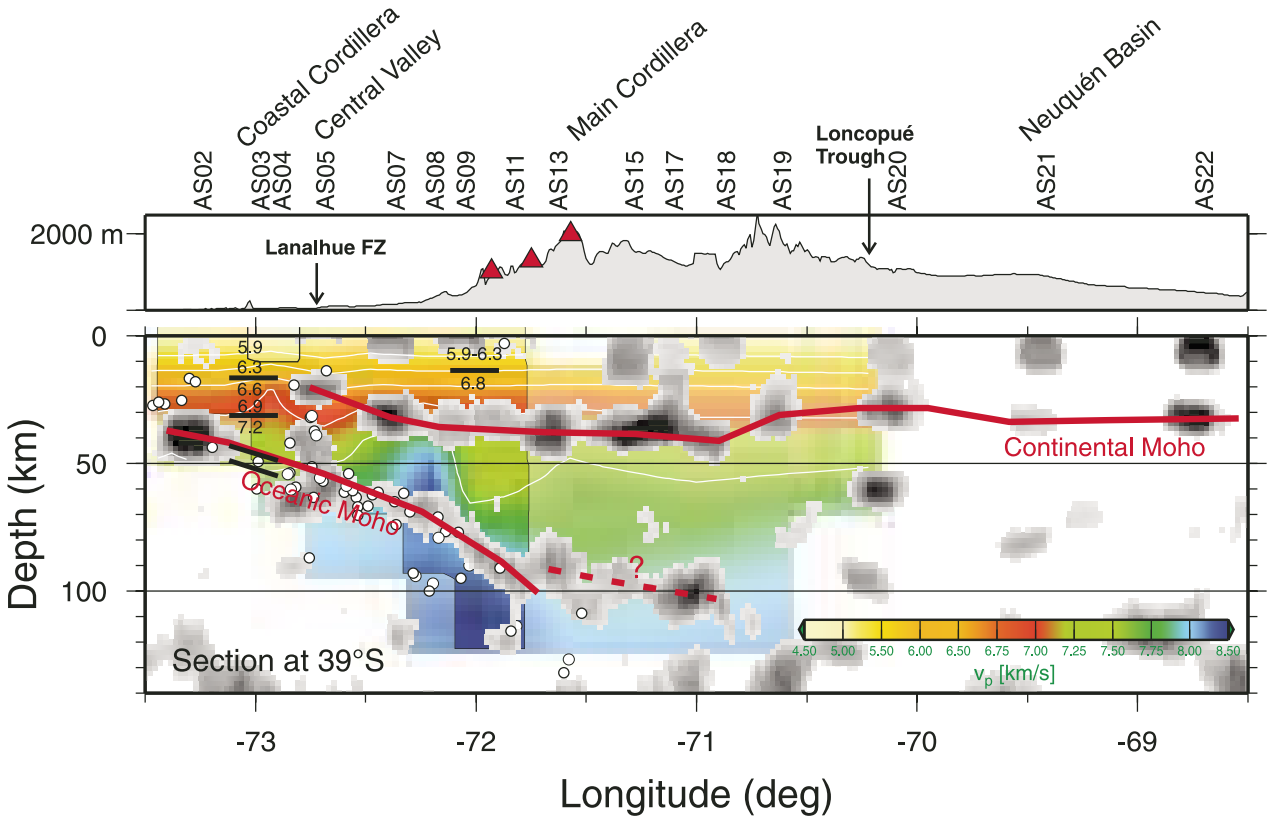

Figure 10. Comparison of receiver functions with results of seismic tomography and seismic refraction. The seismic tomography at latitude 39°S using local earthquakes (Bohm, 2004) has been plotted in color. Thick line segments denote the wide-angle reflections (Bohm et al., 2002; Lüth et al., 2003). P-wave velocities derived from the seismic refraction data are plotted above and below the wide-angle reflections. Receiver functions have been plotted in grayscale. Only positive amplitudes are shown; red solid lines mark the Moho and the slab by receiver functions; red dashed line marks a mysterious subhorizontal interface. FZ—fault zone.

that the Lanalhue fault zone is a lithospheric-scale feature that cuts through the entire upper plate to the subducted slab. Tomography shows a relatively low P-wave velocity immediately above the slab, which may indicate a serpentinized mantle wedge in the cold forearc domain (Bohm, 2004). However, an unequivocal petrophysical interpretation of the complex boundary zone of the upper and lower plate and the active forearc wedge cannot be made on the basis of the presented receiver function imaging.

The wide-angle seismic data was collected in the western part of the profile between 74 and 70°S. The limited data of four shots only show a piece of Moho reflection in the Coastal Cordillera. Elsewhere, the Moho is not seen. An intracrustal interface is detected beneath the Coastal and the Main Cordillera. However, they are not seen in the receiver functions. The absence of the wide-angle reflection of the continental Moho probably reflects the transitional nature of the crust-mantle boundary. A gradient velocity boundary of several kilometers that is detectable by the receiver functions cannot be detected by the short-period wide-angle reflection. Compared to the Central Andes, the average crustal Vp/Vs ratio is apparently higher in the Southern Andes (more than 1.80 in much of the section). The relatively high Vp/Vs ratio would suggest a large amount of mafic lower crust, which could reduce the velocity contrast between the lower crust and the uppermost mantle.

In the eastern part of the section, between 71° and 70°W longitude, the Moho is uplifted by 3–4 km beneath the Loncopué trough in a backarc position. The crustal Poisson's ratio is 0.226 (Vp/Vs ratio of 1.68), slightly lower than normal. The Loncopué trough is a long depression subparallel to the Cordillera and consists of a half-graben system initiated during the Oligocene and extensionally reactivated in the Pliocene-Pleistocene and active until present (Ramos and Folguera, 2005). Based on this, the observed Moho upwelling is interpreted as an initiating rift structure related to active backarc extension.

ACKNOWLEDGMENTS

The work was supported by the Sonderforschungsbereich (SFB) 267 of the Deutsche Forschungsgemeinschaft. Seismic instruments were provided by the GeoForschungsZentrum Potsdam (Geophysical Instrument Pool Potsdam), the Freie Universität Berlin, and the Universität Potsdam. We thank Susan Beck and Eric Sandvol for their constructive reviews.

Downloaded from specialpapers.gsapubs.org on April 9, 2015

REFERENCES CITED

ANCORP (Andean Continental Research Project 1996) Working Group, 2003, Seismic imaging of a convergent continent margin and plateau in the Central Andes: Journal of Geophysical Research, v. 108, 2328, doi: 10.1029/2002JB001771.

Angermann, D., Klotz, J., and Reigber, C., 1999, Space-geodetic estimation of the Nazca–South American Euler vector: Earth and Planetary Science Letter, v. 171, p. 329–334, doi: 10.1016/S0012-821X(99)00173-9.

Beck, S.L., Zandt, G., Myers, S.C., Wallace, T.C., Silver, P.G., and Drake, L., 1996, Crustal thickness variations in the Central Andes: Geology, v. 24, p. 407–410, doi: 10.1130/0091-7613(1996)024<0407:CTVITC>2.3.CO;2.

Bohm, M., 2004, 3-D Lokalbebentomographie der südlichen Anden zwischen 36° und 40° [Ph.D. thesis]: Berlin, Freie Universität Berlin, 135 p.

Bohm, M., Lüth, S., Echtler, H., Asch, G., Bataille, K., Bruhn, C., Rietbrock, A., and Wigger, P., 2002, The Southern Andes between 36° and 40°S latitude: Seismicity and average seismic velocities: Tectonophysics, v. 356, p. 275–289, doi: 10.1016/S0040-1951(02)00399-2.

Cahill, T.A., and Isacks, B.L., 1992, Seismicity and shape of the subducted Nazca plate: Journal of Geophysical Research, v. 97, p. 17,503–17,529.

Franzese, J., Spaletti, L., Pérez, I.G., and Macdonald, D., 2003, Tectonic and paleoenvironmental evolution of Mesozoic sedimentary basins along the Andean foothills of Argentina (32°–54°S): Journal of South American Earth Sciences, v. 16, p. 81–90, doi: 10.1016/S0895-9811(03)00020-8.

Gudmundsson, O., and Sambridge, M., 1998, A regionalized upper mantle (RUM) seismic model: Journal of Geophysical Research, v. 103, p. 7121–7136, doi: 10.1029/97JB02488.

Helffrich, G., 2000, Topography of the transition zone seismic discontinuity: Review of Geophysics, v. 38, p. 141–158, doi: 10.1029/1999RG000060.

Hildreth, W., and Moorbath, S., 1988, Crustal contributions to arc magmatism in the Andes of central Chile: Contributions to Mineralogy and Petrology, v. 98, p. 455–489, doi: 10.1007/BF00372365.

Jordan, T., Burns, W., Veiga, R., Pángaro, F., Copeland, P., Kelley, S., and Mpodozis, C., 2001, Extension and basin formation in the Southern Andes caused by increased convergence rate: A mid-Cenozoic trigger for the Andes: Tectonics, v. 20, p. 308–324, doi: 10.1029/1999TC001181.

Kay, S.M., Burns, W.M., Copeland, P., and Mancilla, O., 2006, this volume, Upper Cretaceous to Holocene magmatism and evidence for transient Miocene shallowing of the Andean subduction zone under the northern Neuquén Basin, *in* Kay, S.M., and Ramos, V.A., eds., Evolution of an Andean margin: A tectonic and magmatic view from the Andes to the Neuquén Basin (35°–39°S lat): Geological Society of America Special Paper 407, doi: 10.1130/2006.2407(02).

Kennett, B.L.N., and Engdahl, E.R., 1991, Travel times for global earthquake location and phase identification: Geophysical Journal International, v. 105, p. 429–465.

Kind, R., Yuan, X., Saul, J., Nelson, D., Sobolev, S.V., Mechie, J., Zhao, W., Kosarev, G., Ni, J., Achauer, U., and Jiang, M., 2002, Seismic images of crust and upper mantle beneath Tibet: Evidence for Eurasian plate subduction: Science, v. 298, p. 1219–1221, doi: 10.1126/science.1078115.

Kirby, S., Engdahl, E.R., and Denlinger, R., 1996, Intermediate depth intraslab earthquakes and arc volcanism as physical expressions of crustal and uppermost mantle metamorphism in subducting slabs, *in* Bebout, G.E., Scholl, D.W., Kirby, S.H., and Platt, J.P., eds., Subduction top to bottom: American Geophysical Union Geophysical Monograph 96, p. 195–214.

Langston, C.A., 1977, Corvallis, Oregon, crustal and upper mantle structure from teleseismic P and S waves: Bulletin of the Seismological Society of America, v. 67, p. 713–724.

Lüth, S., Wigger, P., and ISSA 2000 Working Group, 2003, A crustal model along 39°S from a seismic refraction profile—ISSA 2000: Revista Geológica de Chile, v. 30, p. 83–101.

Mohsen, A., Hofstetter, R., Bock, G., Kind, R., Weber, M., Wylegalla, K., Rümpker, G., and the DESERT Group, 2005, A receiver function study across the Dead Sea Transform: Geophysical Journal International, v. 160, p. 948–960.

Muñoz, J., Troncoso, R., Duhart, P., Crignola, P., Farmer, L., and Stern, C., 2000, The relation of the mid-Tertiary coastal magmatic belt in south-central Chile to the late Oligocene increase in plate convergence rate: Revista Geológica de Chile, v. 27, p. 177–203.

Ramos, V.A., 1999, Plate tectonic setting of the Andean Cordillera: Episodes, v. 22, p. 183–190.

Ramos V.A., and Folguera, A., 2005, Tectonic evolution of the Andes of Neuquén: Constraints derived from the magmatic arc and foreland deformation, *in* Veiga, G.D., Spalletti, L.A., Howell, J.A., and Schwarz, E., The Neuquén Basin, Argentina: Geological Society of London Special Publication 252, p. 15–35.

Ramos, V.A., and Kay, S.M., 2006, this volume, Overview of the tectonic evolution of the southern Central Andes of Mendoza and Neuquén (35°–39°S latitude), *in* Kay, S.M., and Ramos, V.A., eds., Evolution of an Andean margin: A tectonic and magmatic view from the Andes to the Neuquén Basin (35°–39°S latitude): Geological Society of America Special Paper 407, doi: 10.1130/2006.2407(01).

Ramos, V.A., Zapata, T., Cristallini, E., and Introcaso, A., 2004, The Andean thrust system: Latitudinal variations in structural styles and orogenic shortening, *in* McClay, K., ed., Thrust Tectonics and Hydrocarbon Systems: Tulsa, Oklahoma, USA, American Association of Petroleum Geologists Memoir 82, p. 30–50.

Shearer, P.M., 1990, Seismic imaging of upper mantle structure with new evidence for a 520-km discontinuity: Nature, v. 344, p. 121–126, doi: 10.1038/344121a0.

Vinnik, L.P., 1977, Detection of waves converted from P to SV in the mantle: Physics of the Earth and Planetary Interiors, v. 15, p. 39–45, doi: 10.1016/0031-9201(77)90008-5.

Yuan, X., Ni, J., Kind, R., Mechie, J., and Sandvol, E., 1997, Lithospheric and upper mantle structure of southern Tibet from a seismological passive source experiment: Journal of Geophysical Research, v. 102, p. 27,491–27,500, doi: 10.1029/97JB02379.

Yuan, X., Sobolev, S., Kind, R., Oncken, O., Bock, G., Asch, G., Schurr, B., Graeber, F., Rudloff, A., Hanka, W., Wylegalla, K., Tibi, R., Haberland, C., Rietbrock, A., Giese, P., Wigger, P., Röwer, P., Zandt, G., Beck, S., Wallace, T., Pardo, M., and Comte, D., 2000, New constraints on subduction and collision processes in the Central Andes from P-to-S converted seismic phases: Nature, v. 408, p. 958–961, doi: 10.1038/35050073.

Zandt, G., Myers, S.C., and Wallace, T.C., 1995, Crustal and mantle structure across the Basin and Range–Colorado Plateau boundary at 37°N latitude and implications for Cenozoic extensional mechanism: Journal of Geophysical Research, v. 100, p. 10,529–10,548.

Zhu, L., and Kanamori, H., 2000, Moho depth variation in southern California from teleseismic receiver functions: Journal of Geophysical Research, v. 105, p. 2969–2980, doi: 10.1029/1999JB900322.

MANUSCRIPT ACCEPTED BY THE SOCIETY 22 DECEMBER 2005

Printed in the USA

Downloaded from specialpapers.gsapubs.org on April 9, 2015

Geological Society of America Special Papers

Deep seismic images of the Southern Andes

X. Yuan, G. Asch, K. Bataille, et al.

Geological Society of America Special Papers 2006;407; 61-72
doi:10.1130/2006.2407(03)

E-mail alerting services click www.gsapubs.org/cgi/alerts to receive free e-mail alerts when new articles cite this article

Subscribe click www.gsapubs.org/subscriptions to subscribe to Geological Society of America Special Papers

Permission request click www.geosociety.org/pubs/copyrt.htm#gsa to contact GSA.

Copyright not claimed on content prepared wholly by U.S. government employees within scope of their employment. Individual scientists are hereby granted permission, without fees or further requests to GSA, to use a single figure, a single table, and/or a brief paragraph of text in subsequent works and to make unlimited copies of items in GSA's journals for noncommercial use in classrooms to further education and science. This file may not be posted to any Web site, but authors may post the abstracts only of their articles on their own or their organization's Web site providing the posting includes a reference to the article's full citation. GSA provides this and other forums for the presentation of diverse opinions and positions by scientists worldwide, regardless of their race, citizenship, gender, religion, or political viewpoint. Opinions presented in this publication do not reflect official positions of the Society.

Notes

Geological Society of America

THE GEOLOGICAL SOCIETY OF AMERICA